Separation and Purification Technology 348 (2024) 127722

Contents lists available at ScienceDirect

Separation and Purification Technology

journal homepage: www.elsevier.com/locate/seppur

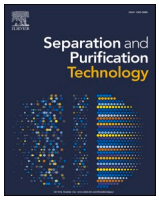

Separation of CO_2/N_2 in Ion-Exchange binder-free beads of zeolite NaY for Post-Combustion CO_2 capture

Ezzeldin Aly [a,b,c,*], Lucas F.A.S. Zafanelli [a,b], Adriano Henrique [a,b], Kristin Gleichmann [d], Alírio E. Rodrigues [e], Francisco A. Da Silva Freitas [c,*], José A.C. Silva [a,b,*]

[a] Centro de Investigação de Montanha (CIMO), Instituto Politécnico de Bragança, Campus Santa Apolónia, 5300-253 Bragança, Portugal
[b] Laboratório Associado para a Sustentabilidade e Tecnologia em Regiões de Montanha (SusTEC), Instituto Politécnico de Bragança, Campus de Santa Apolónia, 5300-253 Bragança, Portugal
[c] Aveiro Institute of Materials, CICECO, Department of Chemical Engineering, University of Aveiro, Campus Universitario de Santiago, 3810-193 Aveiro, Portugal
[d] Chemiewerk Bad Köstritz GmbH, Heinrichshall 2, 07586 Bad Köstritz, Deutschland, Germany
[e] Laboratory of Separation and Reaction Engineering (LSRE), Associate Laboratory LSRE/LCM, Department of Chemical Engineering, Faculty of Engineering, University of Porto, 4099-002 Porto, Portugal

ARTICLE INFO

Keywords:
Binder-free NaY Zeolite
Ion-exchange
Fixed-bed Adsorption
Post-combustion CO_2 Capture
Dynamic Simulations

ABSTRACT

Ion-exchange on bare commercial zeolites can offer improved adsorption processes. In the context of CO_2/N_2 separation for post-combustion CO_2 capture (PCC), here, we report, the effect of ion-exchange on commercial binder-free NaY zeolite with alkali (K^+) and alkaline earth (Ca^{2+}) metal cations, achieving exchange levels of 23 %, 58 %, and 95 % for K^+ and 56 % and 71 % for Ca^{2+}. Adsorption isotherms of CO_2 and N_2 were measured over a temperature range of 306–344 K and pressures up to 350 kPa. At low pressures, the CO_2 adsorption capacity increases as Na^+ ions are exchanged to a higher level of K^+, while a reverse trend is observed for Ca^{2+} exchange. At 25 kPa and 306 K, the CO_2 loading (mol•kg^{-1}) follows the order 2.01-Ca(71)Y < 2.63-Ca(56)Y < 4.05-NaY < 4.29-K(23)Y < 4.59-K(58)Y < 4.72-K(95)Y. The selectivities of CO_2 (15 %)/N_2 (85 %) at 306 K and 101.3 kPa range from 52 for Ca(71)Y to 101 for K(23)Y, compared to 89 in the bare NaY zeolite. The working capacities for the most promising exchanged sample (K(23)Y) exhibit superior values of 4.51, 2.98, and 2.41 mol•kg^{-1} considering regeneration pressures of 3, 10, and 15 kPa, relative to a feed pressure of 101.3 kPa, respectively. Dynamic simulations were conducted using the Aspen Adsorption package to accurately predict both single- and binary-component breakthrough curves.

1. Introduction

Addressing climate change and mitigating its impacts have become global priorities. Carbon dioxide (CO_2) emissions, stemming predominantly from industrial and energy production activities, play a major role in contributing to overall greenhouse gas (GHG) levels [1–3]. Post-combustion capture (PCC) strategies, deployed across sectors such as power generation, steel production, and cement manufacturing, represent technically and economically feasible approaches for mitigating carbon emissions [4–13].

Adsorption-based processes for separating CO_2 from flue gases have undergone extensive study, demonstrating effectiveness across a range of scales, from small-scale plants to large emitters [6,8,14–19]. Solid adsorbents like zeolites hold significant appeal for post-combustion applications owing to their nonvolatile and nontoxic properties, molecular sieving capabilities, operational convenience, cost-effectiveness, reduced environmental impact, and remarkable CO_2 capture capacity and selectivity [4,5,20–24]. A major challenge in PCC is separating the relatively low concentration of CO_2 (approximately 12–15 %) from the large amounts of nitrogen in the flue gas [25,26]. This challenge is surmountable as CO_2 consistently exhibits stronger adsorption than N_2, owing to its larger polarizability and greater quadrupole moment [16].

Zeolites are crystalline aluminosilicate materials with a porous framework consisting of regularly arranged TO_4 tetrahedra, where T represents either silicon (Si) or aluminum (Al). The incorporation of aluminum atoms in the silicate structure introduces negative framework charges, which are counterbalanced by exchangeable cations, typically alkali cations like sodium (Na), potassium (K), calcium (Ca), or magnesium (Mg) located within the pore structure. This arrangement allows

* Corresponding authors.
E-mail addresses: ezzeldin@ipb.pt (E. Aly), fsilva@ua.pt (F.A. Da Silva Freitas), jsilva@ipb.pt (J.A.C. Silva).

https://doi.org/10.1016/j.seppur.2024.127722
Received 1 March 2024; Received in revised form 16 April 2024; Accepted 26 April 2024
Available online 27 April 2024

Nomenclature

a_p	Specific pellet area per unit volume bed of the pellet ($m^2 \bullet m^{-3}$)
b_i	Adsorption affinity constant of component i (bar^{-1})
b_∞	Pre-exponential factor of the affinity constant (bar^{-1})
C	Total gas concentration ($mol \bullet m^{-3}$)
C_i	Feed gas-phase concentration of component i ($mol \bullet m^{-3}$)
C_{io}	Feed gas-phase concentration at the inlet of the fixed bed ($mol \bullet m^{-3}$)
C_{pg}	Specific heat capacity of gas ($J \bullet mol^{-1} \bullet K^{-1}$)
C_{ps}	Specific heat capacity of solid ($J \bullet kg^{-1} \bullet K^{-1}$)
C_{pw}	Specific heat capacity of column wall ($J \bullet kg^{-1} \bullet K^{-1}$)
d_c	Column diameter (m)
d_p	Particle diameter (m)
D_{ax}	Axial dispersion coefficient ($m^2 \bullet s^{-1}$)
D_m	Molecular diffusivity ($m^2 \bullet s^{-1}$)
D_k	Knudsen diffusivity ($m^2 \bullet s^{-1}$)
D_p	Macropore diffusivity ($m^2 \bullet s^{-1}$)
$D_{c,i}$	Intracrystalline diffusivity of component i ($m^2 \bullet s^{-1}$)
$F_{f,i}$	Feed molar flow rate of component i at the inlet of the bed ($mol \bullet m^{-2} \bullet s^{-1}$)
F_i	Feed molar flow rate of component i at the outlet of the bed ($mol \bullet m^{-2} \bullet s^{-1}$)
h_p	Gas-solid heat transfer coefficient ($W \bullet m^{-2} \bullet K^{-1}$)
h_w	Gas-wall heat transfer coefficient ($W \bullet m^{-2} \bullet K^{-1}$)
h_{amb}	Heat transfer coefficient between the wall and the ambience ($W \bullet m^{-2} \bullet K^{-1}$)
k_f	Film mass transfer coefficient ($m \bullet s^{-1}$)
K	Henrýs law equilibrium constant (−)
k_{LDF}	Linear Driving Force coefficient (s^{-1})
K_{ax}	Effective axial bed thermal conductivity ($W \bullet m^{-1} \bullet K^{-1}$)
K_g	Gas phase thermal conductivity ($W \bullet m^{-1} \bullet K^{-1}$)
K_s	Solid phase thermal conductivity ($W \bullet m^{-1} \bullet K^{-1}$)
K_p	Darcy's law proportionality constant ($kg \bullet m^{-3} \bullet s^{-1}$)
K_w	Thermal conductivity of column wall ($W \bullet m^{-1} \bullet K^{-1}$)
m_{ads}	Adsorbent mass in the column (kg)
M_i	Molecular mass of component i ($kg \bullet mol^{-1}$)
Nu	Nusselt number (−)
p_i	Partial pressure of component i (bar)
P	Total pressure of column (bar)
q_i	Adsorbed phase concentration of component i ($mol \bullet kg^{-1}$)
q_i^*	Equilibrium concentration of component i ($mol \bullet kg^{-1}$)
$\overline{q}_i$	Average adsorbed phase concentration of component i ($mol \bullet kg^{-1}$)
Δq_i	Mean relative deviation of adsorbed component i ($mol \bullet kg^{-1}$)
q_m	Maximum adsorbed phase concentration ($mol \bullet kg^{-1}$)
R	Universal gas constant ($J \bullet mol^{-1} \bullet K^{-1}$)
Re	Reynolds number (−)
R_p	Particle radius (m)
r_c	Crystal radius (m)
Sc	Schmidt number (−)
t	Time (s)
t_n	Saturation time (s)
T	Temperature in bulk gas phase (K)
T_s	Temperature in solid phase (K)
T_w	Wall temperature (K)
w_c	Width of column wall (m)
v	Gas phase superficial velocity ($m \bullet s^{-1}$)
v_i	Gas phase interstitial velocity ($m \bullet s^{-1}$)
V_c	Column volume (m^3)
z	Axial coordinate in bed (m)

GREEK LETTERS

$\alpha_{i/j}$	Pure component selectivity of component i over component j (−)
β_i	Working capacity of component i ($mol \bullet kg^{-1}$)
ΔH_i	Heat of adsorption of species i ($kJ \bullet mol^{-1}$)
ΔH_{st}	Isosteric heat of adsorption of species i ($kJ \bullet mol^{-1}$)
λ_f	Film heat transfer coefficient ($W \bullet m^{-2} \bullet K^{-1}$)
ε_b	Bed porosity (−)
ε_p	Particle porosity (−)
ρ_b	Bulk density ($kg \bullet m^{-3}$)
ρ_s	Adsorbent density ($kg \bullet m^{-3}$)
ρ_g	Gas phase molar density ($mol \bullet m^{-3}$)
ρ_w	Wall density ($kg \bullet m^{-3}$)
σ	Collision diameter from the Lennard-Jones potential (Å)
Ω_D	Integral collision coefficient (−)

precise control over pore size and adsorption properties [21,23].

Zeolites are commonly produced in powdered form and require the addition of a binder to form cohesive macroscopic structures like beads or pellets. However, these binders typically do not participate in the adsorption process; instead, they occupy space within the structure, leading to a decrease in adsorption capacity proportional to the amount of binder added, which can reach up to 20 %. Additionally, other factors such as undesirable chemical reactions and unfavorable pore size distributions can also contribute to a reduction in adsorption efficiency [27]. To address these issues, a technology has been developed where the binder undergoes hydrothermal conversion after manufacturing, transforming it into zeolite material. This process results in a material with 100 % zeolite content, enhancing the secondary pore structure, increasing the presence of macropores, improving pore size distribution, and ultimately leading to superior dynamic adsorption properties compared to conventional materials [28–30].

Zeolites X and Y belong to the aluminosilicate molecular sieve family, characterized by a faujasite-type structure (FAU). Their distinguishing characteristic is their Si/Al ratios. For instance, NaX (also known as 13X) zeolite typically has a Si/Al ratio ranging from 1.0 to 1.5, while NaY zeolite exhibits a higher range, typically falling between 1.5 and 3.0.

The FAU framework comprises sodalite cages arranged geometrically in a diamond form, interconnected by hexagonal prisms (double 6-rings), creating a three-dimensional porous channel structure with 12-oxygen ring pore openings measuring approximately 7.4 Å and supercages around 13 Å in size [31]. The FAU framework demonstrates excellent versatility in gas separation applications, particularly through ion exchange and metal impregnation processes. The introduction of specific cations into the structure significantly influences key factors such as the electric field distribution within the pores, accessible pore volume, and adsorption behavior of both polar and non-polar molecules. These effects arise from the electrostatic interactions induced by the ionic surface and acid-base properties of the zeolite framework, ultimately impacting the material's adsorption characteristics [32,33]. Therefore, ion-exchange serves as a valuable tool for customizing the framework structure to achieve enhanced separation performance in PCC applications.

Barthomeuf [34] investigated the basicity of faujasites with alkali metals (Li, Na, K, Rb, Cs) as compensating cations, revealing an increasing basicity with larger cation size, influenced by cation electronegativity. Larger cations like Rb or Cs are expected to have greater

capacities for acidic adsorbates, but smaller cations like Li may exhibit stronger interactions with acidic molecules due to shorter distances available for interaction with the center of mass of the adsorbate CO_2. Barrer and Gibbons [35] found a clear association between cation properties and adsorption strength in X zeolites. Higher charge density cations exhibited stronger adsorption, evident in the order LiX > NaX > KX based on heats of adsorption of CO_2 at low coverage. In line with these findings, LeVan et al. [36] conducted ion exchange experiments with NaX and NaY zeolites, demonstrating that CO_2 adsorption capacities increased as ionic radii of cations decreased, with Li^+ showing the highest adsorption capacities. In a recent study by Pirngruber et al. [37], an opposing trend emerged regarding the adsorption of CO_2 on faujasite Y. The research observed that partial or complete substitution of Na cations with Cs and K cations in Y faujasite resulted in an enhanced adsorption capacity at low pressure. This improvement was primarily attributed to a more favorable adsorption isotherm. Unlike LiY, NaY, and X faujasites, where the polarizing effect was significant, the increased capacity in CsY and KY faujasites was linked to the predominant acid-base interaction between CO_2 and the framework oxygen atoms.

In a separate investigation [38] focusing on the impact of impregnated cations on zeolite 13X, the study revealed that cations like Li^+, K^+, Ca^{2+} and Mg^{2+} introduced into the supports, significantly influenced both the adsorption of CO_2 and the morphological properties of the sorbent. Even with divalent cations, such as Ca^{2+} (0.99 Å), that possess larger ionic radii compared to monovalent cations like Li^+ (0.68 Å), the net area occupied by Ca^{2+} ions is expected to be less due to the replacement of two monovalent ions with a single divalent ion.

Maurin et al. [39] conducted both experimental and theoretical investigations into the CO_2 adsorption capacity and enthalpy for several FAU-type zeolites in their sodium form, with varying Si/Al ratios. The zeolites studied included dealuminated NaY (DAY, Si/Al = 100), NaY (Si/Al = 2.4), and low-silica NaX (NaLSX, Si/Al = 1). The study findings demonstrate that zeolites characterized by smaller Si/Al ratios are expected to exhibit superior adsorption capacity and selectivity for polar molecules [40]. Zeolite with a higher Al content require more cations to balance the charge difference between silicon (Si^{4+}) and aluminum (Al^{3+}), resulting in a more heterogeneous surface and an intensified electrostatic field within the zeolite's pores [16,41]. However, despite their potential for high CO_2 adsorption capacity and selectivity, low silica zeolite materials exhibit poor tolerance to moisture [42–44]. The presence of moisture in cationic zeolites reduces CO_2 capture efficiency by preferentially adsorbing polar H_2O molecules onto exchangeable cations, limiting available adsorption sites for CO_2 [45]. Moisture also weakens the electric field by promoting bicarbonate formation [24,46]. Increasing the Si/Al ratio, as seen in Y zeolites, is an effective way to improve the catalytic and hydrothermal stability by augmenting the zeolite's hydrophobicity. This results in improved stability across various conditions including flue gas and adsorption operations, as well as stability in the presence of water vapor [47,48].

In this study, ion-exchange processes were conducted on commercial binder-free NaY zeolite, introducing varying proportions of K^+ (23 %, 58 %, and 95 %) and Ca^{2+} (56 % and 71 %) with the aim of enhancing its suitability for the separation CO_2/N_2 in PCC applications. Fixed-bed breakthrough experiments were performed across a temperature range of 306 K to 344 K and pressures up to 350 kPa. These experiments aimed to explore the equilibrium, kinetics, and dynamic behavior of the sorption process, including both single and binary mixtures of CO_2 and N_2. Performance parameters including selectivity and working capacity were assessed based on the experimental findings. Subsequently, the collected data were utilized to calibrate a mathematical model using Aspen Adsorption v10 software [49], enabling simulation of fixed-bed performance under typical PCC conditions. Furthermore, a comparative analysis of adsorbent metrics was conducted, comparing binder-free FAU zeolites and a range of other adsorbents documented in the literature [10,13,50–52], such as zeolite 13X, Metal-Organic Frameworks (MOFs), and Activated Carbon.

2. Materials and methods

2.1. Adsorbent and adsorbate

The FAU type-Y zeolites investigated in this study were synthesized in a binder-free form, denoted as Köstrolith NaYBFK, with a Si/Al ratio of 2.5. The synthesis was conducted at the laboratory facilities of *Chemiewerk Bad Köstritz GmbH (Germany)*. The base material NaY was synthesized via a liquid-phase process using sodium silicate, sodium aluminate, and sodium hydroxide, following established industrial procedures [53]. Initially, a temporary binder such as metakaolin was mixed with zeolite powder and shaped using granulation or extrusion techniques. After shaping, the beads were dried, re-moistured, and subjected to aging and hydrothermal conversion in an alkane solution for 16 h at 84 °C. Subsequently, the bulk material was separated, and the crystals underwent washing until reaching a pH value between 9 and 12 in the effluent [27,30]. The zeolite powder, in its base sodium form, then underwent ion exchange.

During the ion exchange process in the liquid phase, either potassium ions or calcium ions were substituted for sodium ions. To achieve this, the granulated sodium form (NaYBFK) was continuously passed through a solution containing water and potassium hydroxide KOH (for potassium ion exchange) or calcium chloride $CaCl_2$ (for calcium ion exchange) with a molarity ranging between 0.027 and 0.55 mol•l^{-1}. This exchange process was conducted within an ion exchange column maintained at a temperature of 298.15 K. Subsequently, the zeolites underwent activation at temperatures ranging from 573.15 K to 673.15 K. The exchange rate refers to the quantity of sodium cations extracted from the base material NaY and replaced with either potassium or calcium cations. The materials in this work have potassium exchange rates of 23 %, 58 %, and 95 %, while the calcium exchange degrees are 56 % and 71 %. Additional details regarding the ion exchange procedures for achieving the exchange rates are detailed in Appendix A5.

Air Liquide supplied the adsorbate and inert gases utilized in this study, with the following specifications: Helium (He) ALPHAGAZ 2 (99.9998 % purity), Carbon Dioxide (CO_2) N48 (99.998 % purity), and Nitrogen (N_2) N50 (99.999 % purity).

2.2. Characterization

The textural properties of the binder-free NaY beads were assessed by N_2 adsorption − desorption using an accelerated surface area and porosimetry system (ASAP® 2420, Micromeritics) at 77 K and pressures up to 101.3 kPa. Prior to the experiments, the samples underwent a 12-hour outgassing at 573 K under vacuum (up to 10^{-7} mbar).

The porosity was assessed through mercury intrusion porosimetry (MIP), conducted using a pore size analyzer (Micromeritics AutoPore IV 9500). The analysis employed a contact angle of 130° and covered the pressure range from 0.003 to 207 MPa, following activation under the previously specified conditions.

The surface morphology of binder-free zeolite NaY was examined using a scanning electron microscopy instrument (JEOL Model JSM-6490) with a high resolution of 3.0 nm.

2.3. Experimental procedure

A single and multicomponent breakthrough apparatus was employed to investigate the dynamics of fixed-bed adsorption involving CO_2 and N_2, alongside obtaining adsorption equilibrium data [54] (Appendix A1). The apparatus configuration is depicted in Fig. A1, and Table A1 provides details on the properties of the fixed bed column and the adsorbents (e.g., weight of adsorbent, beads diameter, etc.). Additionally, it should be noted that potential errors may be associated with the mass flow controller, which has a 2 % margin of error.

To assess the reliability of the methodology and the recyclability of the binder-free zeolites studied in this work, five CO_2 breakthrough experiments were repeated for one of our materials under the same conditions. Following each run, the material underwent cleaning at 473 K with a pure He stream (80 mL·min^{-1}) for a minimum of 2 h. Fig. A2a illustrates the CO_2 breakthrough curves, represented in terms of the normalized molar fraction (yi/yi0) as a function of moles fed per unit mass of the adsorbent. Additionally, Fig. A2b presents the loadings of CO_2 calculated for each run. Notably, the calculated CO_2 loadings for all runs remained consistent, approximately 5.36 mol·kg^{-1}. This consistency serves as evidence of the reliability of the methodology and confirms the material's capability for regeneration and reuse without any loss in capacity.

2.4. Adsorption equilibrium model

The isotherms for both single and multicomponent adsorption were modelled using the dual-site Langmuir (DSL) isotherm (Eq. A2). The choice of the DSL model was motivated by its ability to accurately capture the presence of two distinct adsorption sites within the zeolite framework. These sites are characterized by unique adsorption capacities and affinities [55,56] in FAU zeolite frameworks, as detailed in Appendix A (A2), being well-suited for describing the adsorption behavior of CO_2 and N_2. The DSL fitting of the experimental data was carried out by nonlinear least-squares optimization procedure in which the points were weighted according their estimated errors through Eq. A4.

2.5. Isosteric heats

The isosteric heat (ΔH_{st}) of adsorption was calculated using the Clausius-Clapeyron equation [55,57], which relates to the change in pressure with temperature at constant adsorbed phase concentration, as described in Eq. A5 and A6 within Appendix A [57]. Alternatively, ΔH_{st} can be predicted numerically by the differentiation of the DSL model (as represented by Eq. A7) and detailed in Appendix A3.

2.6. Selectivity, working Capacity, as adsorption performance metrics

The thermodynamic selectivity (α) (or separation factor) of component i over component j refers to the ability of an adsorbent material to preferentially adsorb one component from a mixture of gases and can be defined as [16,58],

$$\alpha_{i/j} = \frac{q_i/q_j}{p_i/p_j} \tag{1}$$

where q_i and q_j are the adsorption equilibrium values of components i and j at the same temperature; p_i and p_j the partial pressures, respectively. To generate the numerical predictions, Eq.1 was employed while incorporating the DSL model (Eq. A2).

The working capacity refers to the amount of gas that an adsorbent can adsorb under specific operating conditions. A general expression including both temperature and pressure for the working capacity is [59]:

$$\beta = q(T_1, P_1) - q(T_2, P_2) \tag{2}$$

where $q(T_1, P_1)$ is the amount adsorbed at temperature T_1 and partial pressure P_1 in the adsorption step, and $q(T_2, P_2)$ is temperature T_2 and regenerating pressure P_2 in the desorption step.

2.7. Breakthrough mathematical modelling

Aspen Adsorption v10 [49] package was used for the numerical simulation of fixed bed adsorption in both single and binary-component breakthrough experiments. Detailed information regarding the mathematical model and the correlations employed for estimating the model parameters can be found in Appendix A4 and Tables A2 and A3. The input data employed in the simulator for single and binary-component adsorption equilibrium studies are derived from the experimental data obtained in the course of this study.

3. Results and discussion

3.1. Adsorbent properties and Characterization

N_2 gas sorption (Fig. 1a), mercury (Hg) intrusion porosimetry (Fig. 1b) and scanning electron microscopy (SEM) (Fig. 1c–f), were employed to determine the textural properties of the adsorbents. The textural data for the bare binder-free NaY are summarized in Table A4. N_2 gas sorption reveals a volume adsorbed of approximately 225 cm^3•g^{-1} at the saturation capacity of the monolayer. The Hg intrusion porosimetry results for binder-free NaY, as depicted in Fig. 1b, illustrate differential intrusion/extrusion concerning pore size diameter, with an average pore size diameter of 10^3 nm, indicating that the majority of pores fall within the macropore size class (according to the IUPAC scheme [60]). SEM images, presented in Fig. 1c–f, reveal crystals with an average size of approximately 1 μm (10^3 nm), displaying cubic/spherical characteristics.

3.2. Adsorption equilibrium of CO_2 and N_2 on ion-exchanged binder-free zeolite Y

The pure component adsorption equilibrium data for CO_2 and N_2 on the series of binder-free FAU zeolites were measured through breakthrough experiments at three temperatures: 306, 326, and 344 K, and five partial pressures: 0.1, 0.25, 0.5, 1.5, and 3.5 bar, relevant for PCC applications. The DSL model fitting parameters are outlined in Table 1.

Fig. 2 presents the adsorption isotherms for CO_2 on bare binder-free NaY zeolite, alongside ion-exchanged zeolites: K(23)Y, K(58)Y, K(95)Y, Ca(56)Y, and Ca(71)Y, across temperatures of 306, 326, and 344 K. The maximum CO_2 loading exceeds 7 mol•kg^{-1} for sample K(23)Y, representing a 4.39 % increase relative to bare commercial NaY.

A sorption hierarchy trend is observed at low pressures up to 50 kPa, with the order being Ca(71)Y < Ca(56)Y < NaY < K(23)Y < K(58)Y < K(95)Y across all temperature ranges studied, as shown in Fig. 3. This hierarchy highlights a significant impact of ion-exchange levels on CO_2 adsorption. At low pressures, the transition of ion-exchange from Na^+ to K^+ correlates with an increase in CO_2 loading, whereas the trend reverses during ion-exchange from Na^+ to Ca^{2+}. For instance, at 25 kPa and 306 K, the CO_2 loading for bare binder-free NaY is 4.05 mol•kg^{-1}, increasing to 4.29 for K(23)Y, 4.59 for K(58)Y, and peaking at 4.72 for K(95)Y. This increase represents a 16.5 % improvement in CO_2 adsorption for K(95)Y compared to bare NaY. In contrast, Ca(56)Y exhibits a loading of 2.63 mol•kg^{-1}, and Ca(71)Y records a lower loading of 2.01 mol•kg^{-1}, indicating that Ca(71)Y adsorbs less than half the amount compared to commercial NaY.

These findings indicate a pronounced affinity between acidic CO_2 molecules and the intrinsic basic properties of zeolites hosting larger monovalent cations, particularly evident at low pressures. The strength of this affinity is influenced by the electronegativity of the cations, impacting the distribution of negative charge among the oxygen atoms within the zeolite framework. Larger cations, such as K^+ (with an ionic radius of 1.33 Å), tend to exhibit reduced charge transfer from neighboring lattice oxygen atoms compared to smaller cations like Na^+ (with an ionic radius of 0.97 Å). Consequently, the oxygen atoms possess a higher negative charge, enhancing their basic characteristics [61]. Oxygen atoms with elevated basicity facilitate the transfer of charge to the carbon atom of CO_2, resulting in stronger interactions [33]. Generally, basic zeolites with strong electropositive attributes exhibit strong adsorption capabilities, especially towards acidic molecules with significant permanent quadrupole moments, such as CO_2 [25].

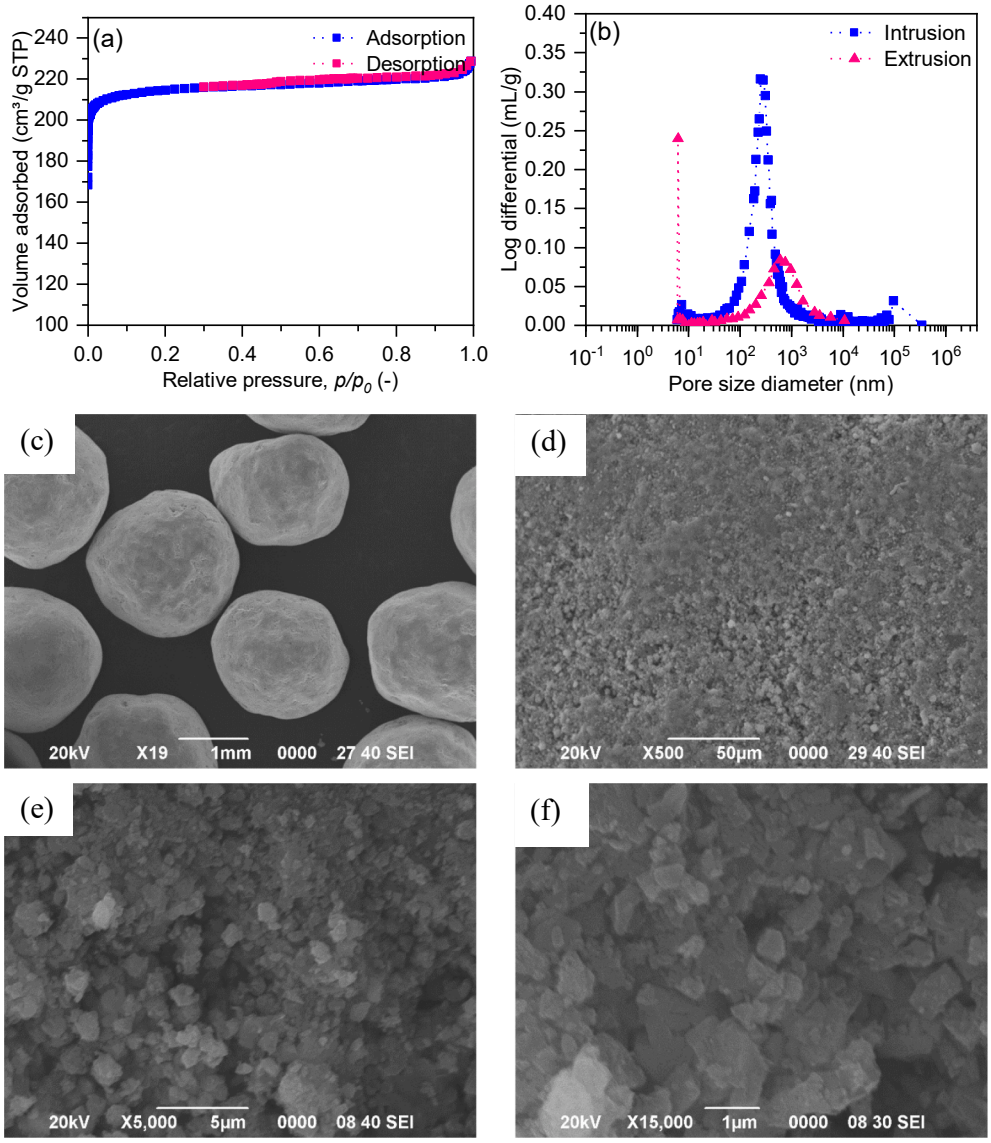

Fig. 1. Characterization: (a) N_2 adsorption equilibrium isotherm at 77 K on binder-free NaY; (b) Differential intrusion and extrusion of Hg in pores on binder-free NaY; (c) SEM images of NaY at various magnifications: (c) × 19, (d) × 500, (e) × 5000, and (f) × 15000.

Additionally, it is noteworthy that the CO_2 loading on Ca(71)Y is substantially lower compared to all other samples, approximately half of that observed on the bare NaY. This effect arises from a decreased availability of exchangeable cations due to the exchange of two monovalent Na^+ cations with a single divalent Ca^{2+} ion. The ion-exchange process from NaY to CaY significantly reduces the number of exchangeable cations, resulting in fewer adsorbent-adsorbate interactions and a consequent decrease in the binding energy of CO_2 molecules.

At pressures exceeding 200 kPa, K(23)Y and NaY exhibit the highest CO_2 loadings, followed by K(58)Y and K(95)Y. The presence of smaller exchangeable cations exerts a positive influence on CO_2 adsorption uptake [62,63]. An acidic molecule with a quadrupole moment is expected to have stronger interactions with smaller cations due to the shorter distances for interaction with the center of mass of the adsorbate [36]. With increasing pressure levels, these smaller cations occupy less volume when compared to their larger counterparts, facilitating the adsorption by accommodating a greater number of CO_2 molecules within the framework cavities. These smaller, polarizing cations have the capacity to effectively permeate channels, establishing stronger ion-quadrupole interactions with CO_2 [64].

The N_2 isotherms, shown in Fig. 4, follow a more linear behavior when compared to CO_2. It exhibits a similar trend in sorption hierarchy to that observed for CO_2 (particularly at low pressures). Nonetheless, the recorded N_2 loadings are significantly lower compared to those of CO_2. At 150 kPa and 306 K, the N_2 observed loadings are only: 0.43 for K(95)Y, 0.39 for K(58)Y, 0.37 for NaY, 0.35 for K(23)Y, 0.32 for Ca(56)Y, and 0.28 mol•kg^{-1} for Ca(71)Y. The observed trend suggests that FAU Y-type zeolites with smaller monovalent cations, like binder-free K(23)Y and NaY, exhibit slightly lower N_2 uptake compared to other K^+ exchanged adsorbents, potentially contributing to higher CO_2/N_2 selectivities and enhancing CO_2 separation efficiency. In industrial applications, there is a consistent preference for materials with high CO_2 and low N_2 loadings to enhance the effectiveness and economic viability in adsorption PCC technologies [4].

Fig. 5 presents the adsorption equilibrium selectivity of CO_2 over N_2 for the studied binder-free FAU Y zeolites. Notably, the CO_2/N_2 selectivities are generally high. At 50 kPa and 326 K, the CO_2/N_2 selectivities are as follows: 35 for NaY, 42 for K(23)Y, 39 for K(58)Y, 32 for K(95)Y, 27 for Ca(56)Y, and 24 for Ca(71)Y. Analysis of CO_2/N_2 selectivity data in Fig. 5(a–c) reveals consistent superior performance by binder-free zeolite K(23)Y across various conditions. For instance, at 306 K and

Table 1
Adsorption equilibrium DSL model parameters for sorption of CO_2 and N_2 on binder-free NaY and ion-exchange K(23)Y, K(58)Y, K(95)Y, Ca(56)Y, and Ca(71)Y zeolites.

Species	q_m(mol•kg^{-1})		b(kPa^{-1})*		ΔH_i(kJ•mol^{-1})	
	q_{m1}	q_{m2}	b_1	b_2	$(\Delta H_i)_1$	$(\Delta H_i)_2$
NaY						
CO_2	3.41	3.93	1.84×10^{-1}	1.75×10^{-2}	−37.6	−34.9
N_2	4.54	–	5.76×10^{-4}	–	−12.8	–
K(23)Y						
CO_2	4.47	3.29	1.44×10^{-1}	1.20×10^{-2}	−38.2	−34.9
N_2	6.68	–	3.64×10^{-4}	–	−13.3	–
K(58)Y						
CO_2	1.23	5.53	1.01×10^{-2}	1.49×10^{-1}	−34.4	−39.1
N_2	2.88	–	1.03×10^{-3}	–	−15.6	–
K(95)Y						
CO_2	2.22	5.28	5.68×10^{-3}	2.02×10^{-1}	−36.4	−41.3
N_2	1.94	–	2.01×10^{-3}	–	−15.9	–
Ca(56)Y						
CO_2	5.55	1.95	8.06×10^{-3}	1.91×10^{-1}	−29.2	−35.1
N_2	1.68	–	1.59×10^{-3}	–	−14.1	–
Ca(71)Y						
CO_2	1.97	5.40	9.94×10^{-2}	4.9×10^{-3}	−32.6	−28.4
N_2	3.05	–	6.94×10^{-4}	–	−15.5	–

* The reference temperature used is 306 K.

50 kPa, the CO_2/N_2 selectivity for K(23)Y is 41, surpassing those of NaY (38), K(58)Y (35), K(95)Y (28), Ca(56)Y (26), and Ca(71)Y (24). This sustained elevation highlights K(23)Y's notable proficiency in preferentially adsorbing CO_2 over N_2, suggesting potential applicability in adsorption PCC processes.

In Fig. 6, the numerically predicted isosteric heats using the DSL model (Eq. A7), are compared to the experimental values (Eq. A6) for (a) CO_2 and (b) N_2 across all investigated binder-free FAU zeolites. The observed isosteric heats for CO_2 are higher than that of N_2, with values ranging from 41.2 to 28.5 kJ•mol^{-1} for CO_2, to 15.6 to 12.8 kJ•mol^{-1} for N_2. For more strongly quadrupolar and dipolar molecules, there is a pronounced decrease in the heat of adsorption with coverage [65]. CO_2 is distinguished by a high quadrupole moment, and the interaction between the field gradient and the quadrupole contributes substantially to the adsorption energy [44]. On the other hand, N_2 is a nonpolar molecule, lacking significant dipole or quadrupole moment. Consequently, its interactions with the adsorbents are less pronounced compared to CO_2, leading to lower isosteric heat values that remain constant with an increase in loading, as evident in Fig. 6b. The observed disparity in the trends of isosteric heats between N_2 and CO_2 highlights the distinct sorbate-sorbent interactions influenced by the differing molecular properties of each gas, thereby contributing to their unique adsorption behaviors on the adsorbents.

The decrease in the heat of adsorption observed across all samples for CO_2 (Fig. 6a) is indicative of the presence of energetic heterogeneity within the zeolite cavities. This phenomenon gives evidence to interactions between the adsorbate and adsorbent, specifically emphasizing the role played by cations in conjunction with the electric field generated by oxygen atoms within the zeolite framework [65,66]. Higher isosteric heat values indicate stronger interactions between cations and CO_2 molecules, suggesting more robust binding forces. The impact of cation exchange becomes more pronounced with higher rates of K^+ cation exchange, leading to elevated isosteric heats at zero coverage. For instance, at 95 % K^+ exchange rate, the isosteric heat reaches approximately 41.3 kJ•mol^{-1}, with a subsequent gradual decrease observed at lower exchange rates. In contrast, Ca^{2+} exhibits considerably lower isosteric heat values, indicating weaker interactions with CO_2. This observation aligns with the reduced availability of exchangeable cations resulting from the exchange of two monovalent Na^+ cations with one divalent Ca^{2+} cation. This process leads to a depopulation of exchangeable cations and a decrease in the amplitude of the electric field within the zeolite cavities [67]. Despite their stronger

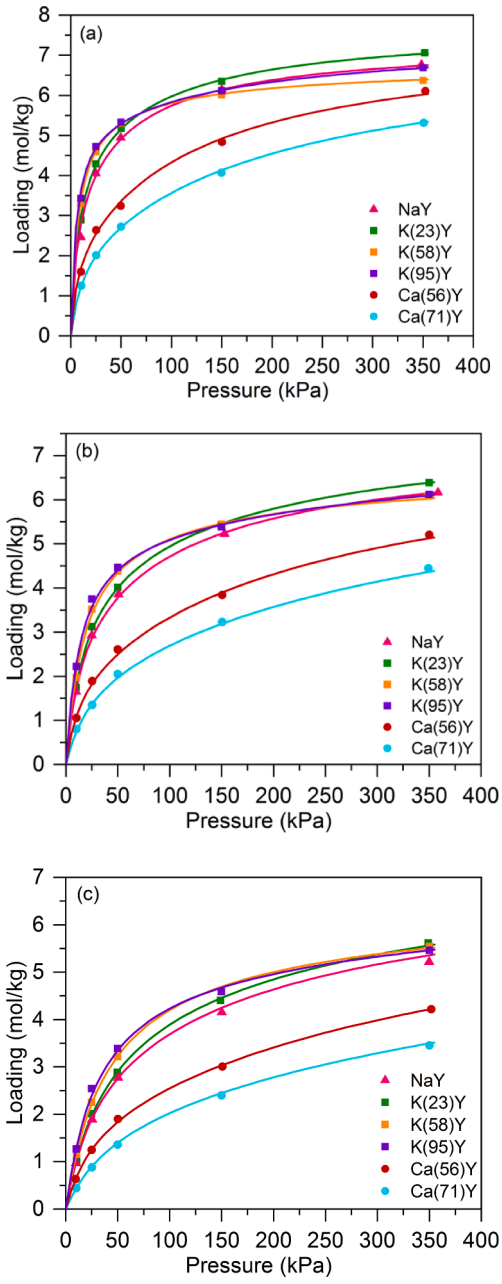

Fig. 2. Comparison of CO_2 adsorption isotherms at (a) 306, (b) 326, and (c) 344 K among binder-free NaY, K(23)Y, K(58)Y, K(95)Y, Ca(56)Y, and Ca(71)Y zeolite. Experimental = symbols; DSL isotherm = lines.

electric fields, divalent cations are typically only half as abundant as monovalent cations and are often situated in less accessible locations [68].

3.3. Binary adsorption experiments for CO_2/N_2 mixtures under typical PCC operating conditions and CO_2 Loadings, selectivities and working capacities

Binary breakthrough experiments were conducted on all binder-free FAU zeolites under standard PCC conditions comprising mixtures with 15 % CO_2 and 85 % N_2 by mol•mol^{-1} at 101.3 kPa and 306 K. The evaluation of CO_2 separation efficiency for the investigated materials followed established methodologies [16,58,69], wherein various adsorbent metrics, including CO_2 loadings, selectivities, and working capacities, were calculated. The comparative analysis, as outlined in

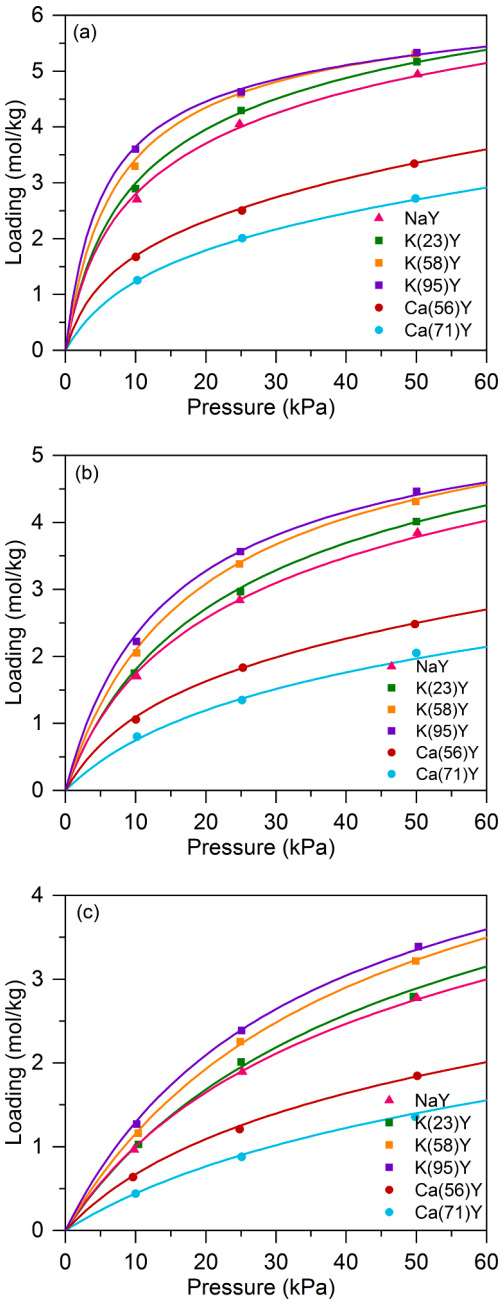

Fig. 3. Comparison of CO_2 adsorption isotherms in the low-pressure range at (a) 306, (b) 326, and (c) 344 K among binder-free NaY, K(23)Y, K(58)Y, K(95)Y, Ca(56)Y, and Ca(71)Y zeolite. Experimental = symbols; DSL isotherm = lines.

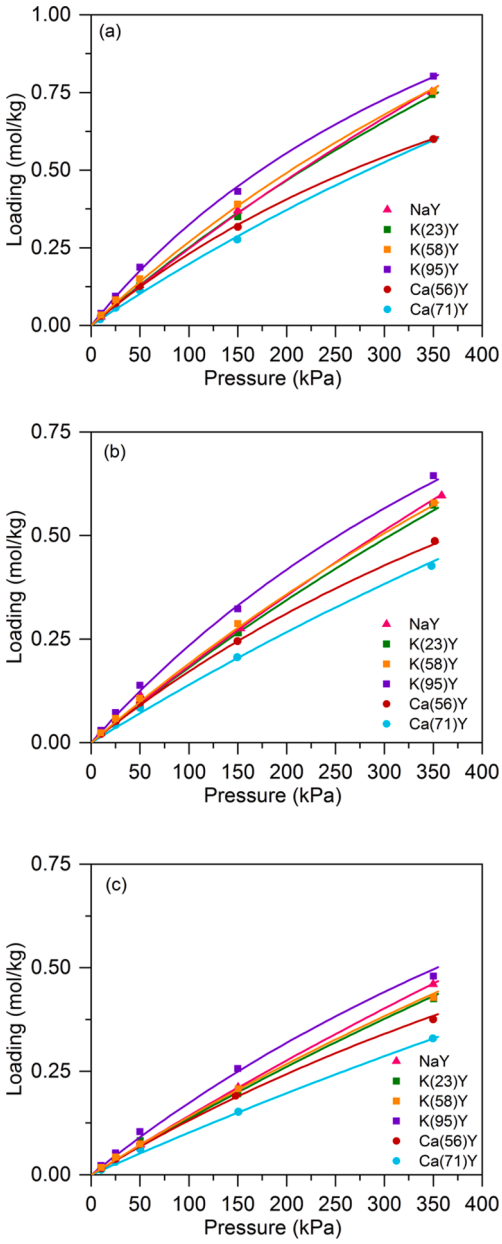

Fig. 4. Comparison of N_2 adsorption isotherms at (a) 306, (b) 326, and (c) 344 K among binder-free NaY, K(23)Y, K(58)Y, K(95)Y, Ca(56)Y, and Ca(71)Y zeolite. Experimental = symbols; DSL isotherm = lines.

Table 2, indicates the binary CO_2 loading and CO_2/N_2 selectivity for K^+ ion-exchange samples as follows: 3.53 mol•kg^{-1} and 101 for K(23)Y, 3.97 mol•kg^{-1} and 97 for K(58)Y, and 4.12 mol•kg^{-1} and 83 for K(95)Y.

Furthermore, working capacity values for CO_2 were calculated across a pressure range proper for Vacuum Swing Adsorption (VSA) PCC processes, considering regeneration pressures of 3, 10, and 15 kPa, relative to a feed pressure of 101.3 kPa, as previously studied elsewhere [8,9,70]. In these calculations, a CO_2 molar fraction of 15 % in the feed and 90 % during regeneration was assumed to align with realistic operational conditions. Fig. 7 presents a comparison of CO_2 working capacities for all materials under the previously mentioned conditions. The results demonstrate that all investigated binder-free K^+ exchanged zeolites surpass both the bare binder-free NaY and benchmark zeolite 13X, highlighting the significance of this ion-exchange study. In the pressure range of 3 to 101.3 kPa, binder-free K(23)Y exhibits the highest CO_2 working capacity at 2.37 mol•kg^{-1}, surpassing NaY by 15.2 %, K(58)Y by 7.17 %, K(95)Y by 5.06 %, Ca(56)Y by 46.8 %, and Ca(71)Y by 55.3 %. Additionally, the CO_2/N_2 working selectivity was assessed for each adsorbent under identical conditions, as detailed in Table A8. Notably, binder-free K(23)Y consistently exhibits superior working selectivity across all temperatures. At 326 K, the working selectivity equals 77, representing a 16.3 % increase over NaY, a 0.92 % increase over K(58)Y, a 25 % increase over K(95)Y, an 81.6 % increase over Ca(56)Y, and an 84.7 % increase over Ca(71)Y.

Considering the studied adsorbent metrics, binder-free K(23)Y emerge as a well-rounded performer in CO_2 separation from flue gas, demonstrating notable performance in terms of loading, selectivity, and working capacity across various operational conditions.

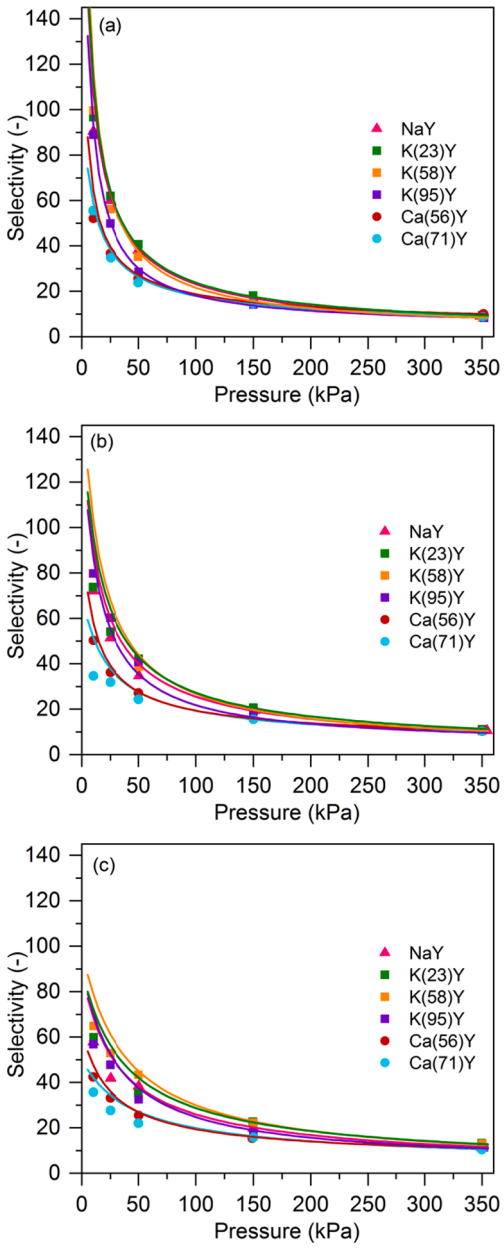

Fig. 5. Selectivity of CO_2/N_2 at (a) 306, (b) 326, and (c) 344 K as a function of pressure for binder-free NaY, K(23)Y, K(58)Y, K(95)Y, Ca(56)Y, and Ca(71)Y zeolite. Experimental = symbols; Numerical (DSL model) = lines.

3.4. Modeling of CO_2 Single-Component breakthrough experiments

The modeling of breakthrough curves is pivotal in gaining a physical understanding of the dynamic behavior in these experiments, which is essential for the design of cyclic adsorption processes [71]. Aspen Adsorption was employed to simulate the dynamics of fixed bed adsorption breakthrough experiments. Details regarding the mathematical model and correlations can be found in Appendix A4 and Tables A2 and A3.

Fig. 8 presents the experimental and simulated single-component breakthrough curves, represented as mole fractions normalized by the component mole fraction in the feed, for CO_2 adsorption on binder-free NaY zeolite at a partial pressure of 0.5 bar and temperatures of (a) 306 K, (b) 326 K, and (c) 344 K. The transport parameters for the pure-component CO_2 dynamic simulations are presented in Table A5. The experimental and simulated temperature fronts positioned at the

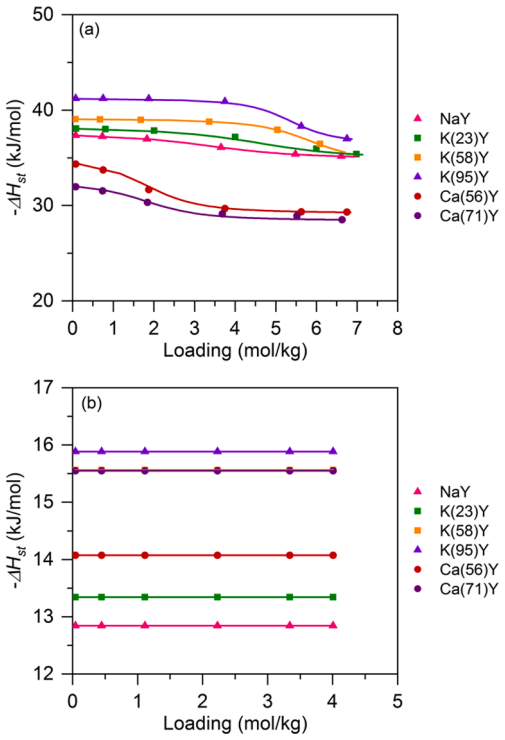

Fig. 6. Isosteric heats of sorption plotted against loading for (a) CO_2 and (b) N_2. Experimental (Eq. A6) = symbols; Numerical (Eq. A7) = lines.

midpoint of the column, are presented on the right Y-axis. As expected, shorter breakthrough times are observed with increasing temperature, accompanied by a decrease in the height of temperature peaks across all temperature conditions. This trend is attributed to the higher heat of adsorption and increased CO_2 adsorption at lower temperatures. Comparing the experimental measurements with the simulation results indicates a strong alignment with the predictive model and the estimated correlations. The mathematical model on Aspen Adsorption effectively reproduces both the height and timing of temperature fronts, as well as the composition curve, being a valuable tool for the design of cyclic adsorption processes using FAU Y-type zeolites in PCC applications.

3.5. Modeling of Binary-Component breakthrough experiments for CO_2/N_2 mixture

The earlier comparative analysis in Table 2 and Fig. 7 established the potential of binder-free K(23)Y as a promising adsorbent for CO_2 separation from flue gas. Fig. 9 presents the simulated and experimental breakthrough curves and temperature fronts for binary CO_2/N_2 adsorption in binder-free K(23)Y at temperatures of (a) 306, (b) 326, and (c) 344 K. The corresponding transport parameters are detailed in Table A6. The simulations conducted in Aspen Adsorption exhibit close alignment with experimental outcomes, affirming the precision of the mathematical model.

The breakthrough curves are illustrated in greater detail in Fig. 10, providing a zoomed-in view that reveals a sharply defined curve, suggesting minimal diffusional limitations within the system. To substantiate this observation, a parametric study (detailed in Appendix A4) was conducted to evaluate the roles of axial dispersion and mass transfer resistances. Firstly, the relative time constant values associated with each term contributing to the overall effective rate coefficient k' (Eq. A9) were calculated compared to determine the primary mechanism influencing the dispersion of mass transfer zones. Subsequently, mathematical simulations were performed using Aspen Adsorption, where the overall mass-transfer coefficient was held constant while axial

Table 2
Comparison of adsorbent metrics between different zeolites samples under PCC conditions.

Binder-free Zeolites	Flue Gas Conditions: CO_2/N_2 (15/85 mol. %), 306 K at 101.3 kPa					
	Binary CO_2 loading q_{bCO2}(mol•kg^{-1})	Pure CO_2/N_2 selectivity α_{CO_2/N_2}(−)	Working capacity β_1(mol•kg^{-1})	Working capacity β_2(mol•kg^{-1})	Working capacity β_3(mol•kg^{-1})	Ref.
NaY	3.29	89	2.01	0.66	0.14	*
K(23)Y	3.53	101	2.37	0.71	0.15	*
K(58)Y	3.97	97	2.20	0.71	0.14	*
K(95)Y	4.12	83	2.25	0.63	0.12	*
Ca(56)Y	1.98	58	1.26	0.44	0.09	*
Ca(71)Y	1.52	52	1.06	0.39	0.09	*
Other adsorbents						
Zeolite 13X	3.14	80	1.28	0.41	0.09	[13]
Mg-MOF-74	6.07	52	2.26	0.53	0.10	[50]
UTSA-16	1.64	152	1.65	0.61	0.13	[51]
CS-AS	0.77	17	0.76	0.35	0.08	[52]

Conditions:
β_1 ads: q (T1, P1) = q (306 K, 101.3 kPa). β_1 des: q (T2, P2) = q (306 K, 3 kPa).
β_2 ads: q (T1, P1) = q (306 K, 101.3 kPa). β_2 des: q (T2, P2) = q (306 K, 10 kPa).
β_3 ads: q (T1, P1) = q (306 K, 101.3 kPa). β_3 des: q (T2, P2) = q (306 K, 15 kPa).
* Data measured in this work.

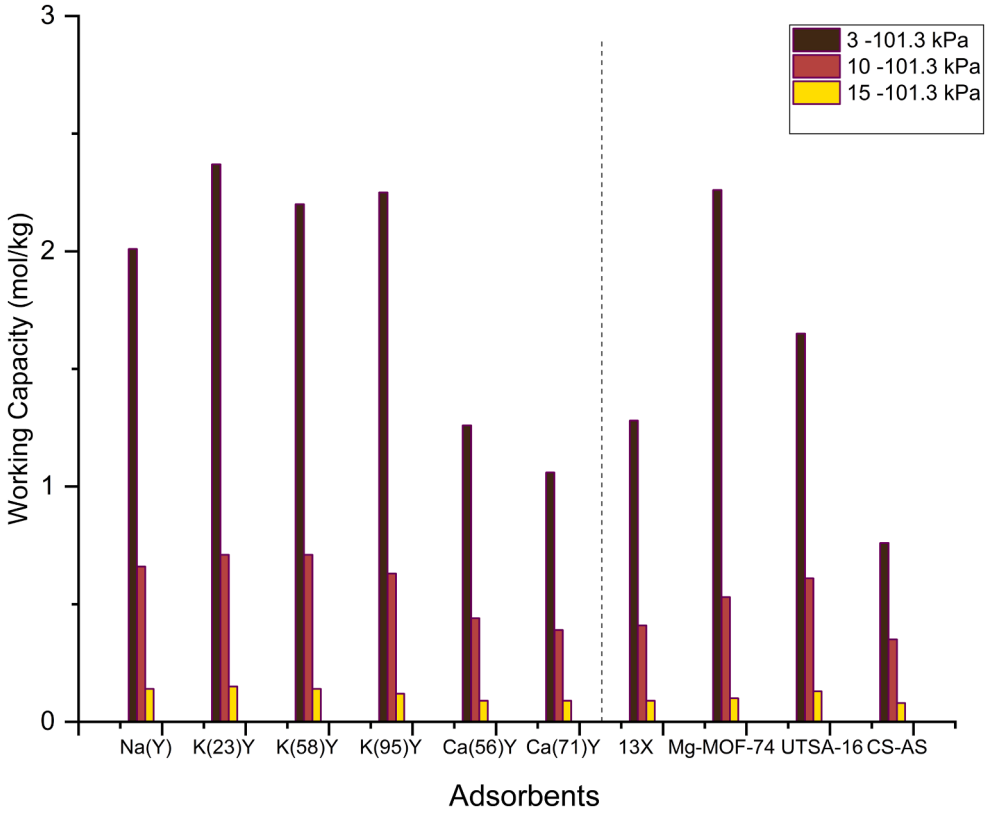

Fig. 7. Comparison of CO_2 working capacities at 306 K across different PCC operating scenarios, including regeneration pressures of 3, 10, and 15 kPa, relative to a feed pressure of 101.3 kPa. Adsorbents depicted to the left of the dotted vertical line represent materials investigated in this study.

dispersion was varied (Fig. A3a), and then conversely (Fig. A3b). The results of this study indicate that axial dispersion predominantly governs zone spreading within the bed in all experiments.

4. Conclusions

Adsorption equilibrium measurements of CO_2 and N_2 were conducted on a range of ion-exchanged binder-free FAU type-Y zeolites through a set of fixed bed breakthrough experiments. The CO_2 adsorption capacities at low pressures followed the trend: Ca(71)Y < Ca(56)Y < NaY < K(23)Y < K(58) < K(95)Y. The N_2 sorption behavior suggests that Y-type zeolites with smaller monovalent cations, like binder-free K(23)Y and NaY, exhibit slightly lower N_2 uptake compared to other K^+ exchanged adsorbents, thereby contributing to the higher CO_2/N_2 selectivities.

Binary-component experiments involving a CO_2/N_2 mixture highlight the potential of binder-free K(23)Y as an effective adsorbent for CO_2 recovery from post-combustion streams. With a CO_2 loading capacity of 3.53 mol•kg^{-1} and a selectivity of approximately 101 over N_2. Furthermore, the binder-free K(23)Y bead demonstrated noteworthy

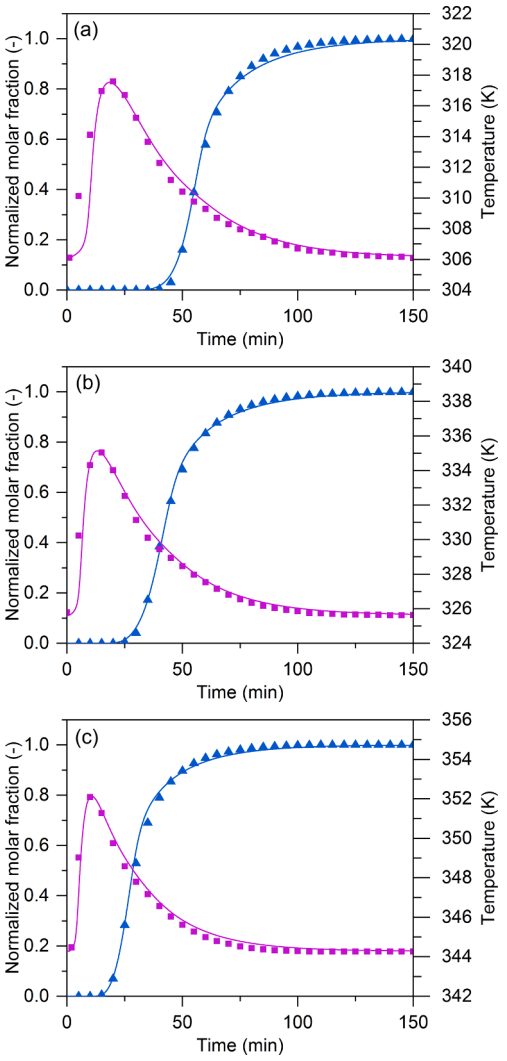

Fig. 8. Breakthrough curves (▲) and temperature fronts at the middle position of the bed (■) for binder-free NaY zeolite in pure CO_2 fixed bed experiments at (a) 306, (b) 326, and (c) 344 K and 0.5 bar partial pressure. Experimental = symbols; Aspen numerical predictions = lines.

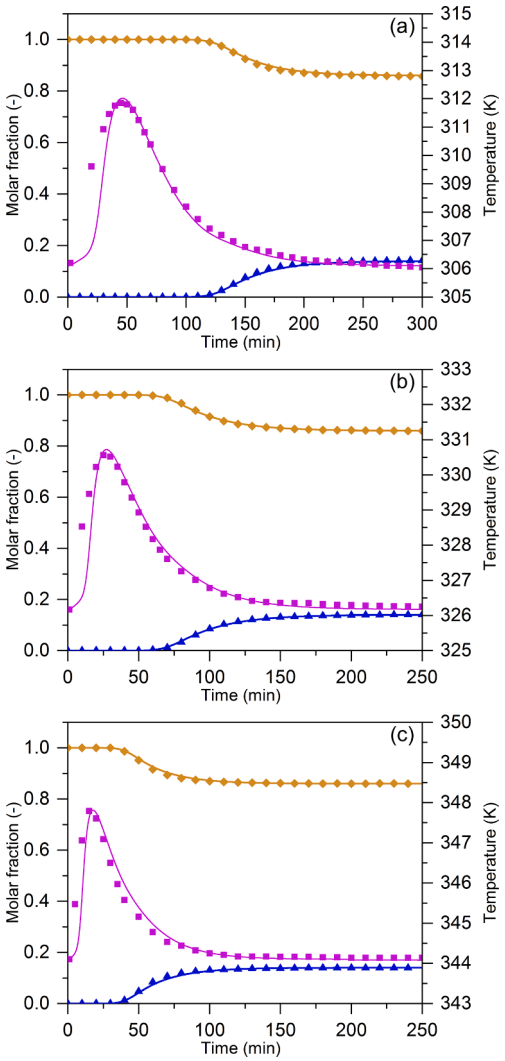

Fig. 9. Breakthrough curves for binder-free K(23)Y zeolite in binary CO_2 (15 %) (▲) and N_2 (85 %)(◆) fixed bed experiments and temperature fronts (■) at (a) 306, (b) 326, and (c) 344 K. Experimental = symbols; Aspen numerical predictions = lines.

working capacity in CO_2 separation from flue gas under typical VSA processes, surpassing alternative adsorbents in the literature such as 13X (with binder) by 85.1 %, UTSA-16 by 43.6 %, and Mg-MOF-74 by 4.87 % in the regeneration pressure of 3 kPa relative to a feed pressure of 101.3 kPa.

The findings from this study demonstrate the significant promise of binder-free K(23)Y as a prospective adsorbent for the separation of CO_2 from post-combustion streams. However, it is important to carefully evaluate the associated costs, technical challenges, and intended applications before considering its implementation, despite its improved performance compared to bare NaY.

The data presented in this research are currently being employed in the development of a comprehensive cyclic process aimed at enhancing the practical application and efficiency of this adsorption system for CO_2 recovery using FAU Y-type zeolites.

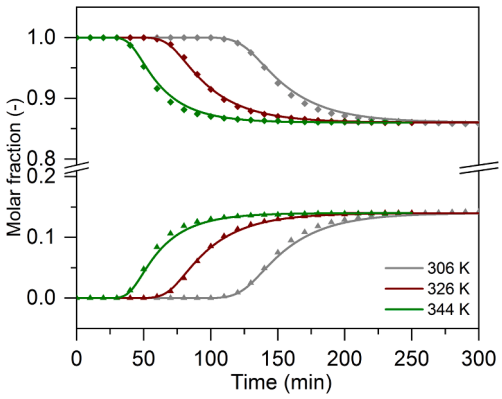

Fig. 10. Breakthrough curves for binder-free K(23)Y zeolites in binary CO_2 (15 %)(▲) and N_2 (85 %)(◆) fixed bed experiments at 306, 326, and 344 K. Experimental = symbols; Aspen numerical predictions = lines.

CRediT authorship contribution statement

Ezzeldin Aly: Writing – review & editing, Writing – original draft, Methodology, Investigation, Formal analysis, Data curation, Conceptualization. **Lucas F.A.S. Zafanelli:** Methodology. **Adriano Henrique:** Methodology. **Kristin Gleichmann:** Writing – review & editing, Resources, Methodology, Conceptualization. **Alírio E. Rodrigues:** Writing – review & editing, Supervision, Methodology, Formal analysis. **Francisco A. Da Silva Freitas:** Writing – review & editing, Supervision,

Methodology, Data curation. **José A.C. Silva:** Writing – review & editing, Writing – original draft, Supervision, Methodology, Formal analysis, Data curation, Conceptualization.

Declaration of competing interest

The authors declare that they have no known competing financial interests or personal relationships that could have appeared to influence the work reported in this paper.

Data availability

Data will be made available on request.

Acknowledgments

This work was supported by national funds through FCT/MCTES (PIDDAC): (1) project PTDC/EQU-EPQ/0467/2020 (DOI:10.54499/PTDC/EQU-EPQ/0467/2020); (2) CIMO, UIDB/00690/2020 (DOI: 10.54499/UIDB/00690/2020) and SusTEC, LA/P/0007/2020 (DOI: 10.54499/LA/P/0007/2020); (3) CICECO -Aveiro Institute of Materials, UIDB/50011/2020 & UIDP/50011/2020 & LA/P/0006/2020.

Appendix A. Supplementary data

Supplementary data to this article can be found online at https://doi.org/10.1016/j.seppur.2024.127722.

References

[1] H. Ritchie, M. Roser, Sector by sector: where do global greenhouse gas emissions come from? Our World Data (2023).
[2] H. Ritchie, P. Rosado, M. Roser, Emissions by sector, Our World Data (2023).
[3] I.C. Change, Mitigation of climate change, Contribution of working group III to the fifth assessment report of the intergovernmental panel on climate change 1454 (2014) 147, https://doi.org/10.1017/cbo9781107415416.
[4] A. Sayari, Y. Belmabkhout, R. Serna-Guerrero, Flue gas treatment via CO2 adsorption, Chem. Eng. J. 171 (2011) 760–774.
[5] S. Choi, J.H. Drese, C.W. Jones, Adsorbent materials for carbon dioxide capture from large anthropogenic point sources, ChemSusChem 2 (2009) 796–854, https://doi.org/10.1002/cssc.200900036.
[6] S.E. Zanco, J.-F. Pérez-Calvo, A. Gasós, B. Cordiano, V. Becattini, M. Mazzotti, Postcombustion CO2 capture: a comparative techno-economic assessment of three technologies using a solvent, an adsorbent, and a membrane, ACS Eng. Au 1 (2021) 50–72, https://doi.org/10.1021/acsengineeringau.1c00002.
[7] F. Raganati, F. Miccio, P. Ammendola, Adsorption of carbon dioxide for post-combustion capture: a review, Energy & Fuels 35 (2021) 12845–12868, https://doi.org/10.1021/acs.energyfuels.1c01618.
[8] Z. Liu, L. Wang, X. Kong, P. Li, J. Yu, A.E. Rodrigues, Onsite CO2 capture from flue gas by an adsorption process in a coal-fired power plant, Ind. Eng. Chem. Res. 51 (2012) 7355–7363, https://doi.org/10.1021/ie3005308.
[9] G. Li, P. Xiao, P. Webley, J. Zhang, R. Singh, M. Marshall, Capture of CO2 from high humidity flue gas by vacuum swing adsorption with zeolite 13X, Adsorption 14 (2008) 415–422, https://doi.org/10.1007/s10450-007-9100-y.
[10] B.J. Maring, P.A. Webley, A new simplified pressure/vacuum swing adsorption model for rapid adsorbent screening for CO2 capture applications, Int. J. Greenh. Gas Control 15 (2013) 16–31, https://doi.org/10.1016/j.ijggc.2013.01.009.
[11] R.M. Siqueira, G.R. Freitas, H.R. Peixoto, J.F. do Nascimento, A.P.S. Musse, A.E. B. Torres, D.C.S. Azevedo, M. Bastos-Neto, Carbon Dioxide Capture by Pressure Swing Adsorption, Energy Procedia 114 (2017) 2182–2192, https://doi.org/10.1016/j.egypro.2017.03.1355.
[12] Z. Liu, C.A. Grande, P. Li, J. Yu, A.E. Rodrigues, Multi-bed Vacuum Pressure Swing Adsorption for carbon dioxide capture from flue gas, Sep. Purif. Technol. 81 (2011) 307–317, https://doi.org/10.1016/j.seppur.2011.07.037.
[13] R. Haghpanah, R. Nilam, A. Rajendran, S. Farooq, I.A. Karimi, Cycle synthesis and optimization of a VSA process for postcombustion CO2 capture, AIChE J. 59 (2013) 4735–4748, https://doi.org/10.1002/aic.14192.
[14] V.R. Rao, S. Krishnamurthy, S.K. Guntuka, A. Rajendran, M.A. Ullah, P. Sharratt, I. A. Karimi, S. Farooq, A pilot plant study of a VSA process for CO2 capture from power plant flue gas, 2012.
[15] K.T. Chue, J.N. Kim, Y.J. Yoo, S.H. Cho, R.T. Yang, Comparison of activated carbon and zeolite 13X for CO2 recovery from flue gas by pressure swing adsorption, Ind. Eng. Chem. Res. 34 (1995) 591–598.
[16] P.J.E. Harlick, F.H. Tezel, An experimental adsorbent screening study for CO2 removal from N2, Microporous Mesoporous Mater. 76 (2004) 71–79, https://doi.org/10.1016/j.micromeso.2004.07.035.
[17] W. Shao, L. Zhang, L. Li, R.L. Lee, Adsorption of CO2 and N2 on synthesized NaY zeolite at high temperatures, Adsorption 15 (2009) 497–505, https://doi.org/10.1007/s10450-009-9200-y.
[18] S. Sjostrom, H. Krutka, T. Starns, T. Campbell, Pilot test results of post-combustion CO2 capture using solid sorbents, Energy Procedia 4 (2011) 1584–1592, https://doi.org/10.1016/j.egypro.2011.02.028.
[19] V.P. Mulgundmath, F.H. Tezel, T. Saatcioglu, T.C. Golden, Adsorption and separation of CO 2/N 2 and CO 2/CH 4 by 13X zeolite, Can. J. Chem. Eng. 90 (2012) 730–738, https://doi.org/10.1002/cjce.20592.
[20] A.L. Chaffee, G.P. Knowles, Z. Liang, J. Zhang, P. Xiao, P.A. Webley, CO2 capture by adsorption: materials and process development, Int. J. Greenh. Gas Control 1 (2007) 11–18.
[21] A. Samanta, A. Zhao, G.K.H. Shimizu, P. Sarkar, R. Gupta, Post-combustion CO2 capture using solid sorbents: a review, Ind. Eng. Chem. Res. 51 (2012) 1438–1463.
[22] J. Rouquerol, F. Rouquerol, P. Llewellyn, G. Maurin, K. Sing, Adsorption by powders and porous solids: principles, methodology and applications, Academic press, 2013.
[23] Q. Wang, J. Luo, Z. Zhong, A. Borgna, CO2 capture by solid adsorbents and their applications: current status and new trends, Energy Environ. Sci. 4 (2011) 42–55, https://doi.org/10.1039/C0EE00064G.
[24] M. Younas, M. Sohail, L.K. Leong, M.J.K. Bashir, S. Sumathi, Feasibility of CO2 adsorption by solid adsorbents: a review on low-temperature systems, Int. J. Environ. Sci. Technol. 13 (2016) 1839–1860, https://doi.org/10.1007/s13762-016-1008-1.
[25] C. Chao, Y. Deng, R. Dewil, J. Baeyens, X. Fan, Post-combustion carbon capture, Renew. Sustain. Energy Rev. 138 (2021) 110490.
[26] H. Herzog, What future for carbon capture and sequestration? Environ. Sci. Technol. 35 (2001) 148A.
[27] K. Gleichmann, B. Unger, A. Brandt, Industrial zeolite molecular sieves, in: Zeolites-Useful Minerals, Intech, 2016, p. 13, https://doi.org/10.5772/57353.
[28] D.W. Breck, Zeolite Molecular Sieves: Structure, Chemistry, and Use, Wiley, 1973.
[29] J.A.C. Silva, K. Schumann, A.E. Rodrigues, Sorption and kinetics of CO2 and CH4 in binderless beads of 13X zeolite, Microporous Mesoporous Mater. 158 (2012) 219–228, https://doi.org/10.1016/j.micromeso.2012.03.042.
[30] K. Schumann, B. Unger, A. Brandt, F. Scheffler, Investigation on the pore structure of binderless zeolite 13× shapes, Microporous Mesoporous Mater. 154 (2012) 119–123, https://doi.org/10.1016/j.micromeso.2011.07.015.
[31] L.B. McCusker, C. Baerlocher, Chapter 3 Zeolite structures, in: Studies in surface science and catalysis, Vol. 137, Elsevier, 2001, pp. 37–67, https://doi.org/10.1016/S0167-2991(01)80244-5.
[32] O. Talu, S.Y. Zhang, D.T. Hayhurst, Effect of cations on methane adsorption by NaY, MgY, CaY, SrY, and BaY zeolites, J. Phys. Chem. 97 (1993) 12894–12898, https://doi.org/10.1021/j100151a043.
[33] D. Barthomeuf, Framework induced basicity in zeolites, Microporous Mesoporous Mater. 66 (2003) 1–14.
[34] D. Barthomeuf, Conjugate acid-base pairs in zeolites, J. Phys. Chem. 88 (1984) 42–45.
[35] R.M. Barrer, R.M. Gibbons, Zeolitic carbon dioxide: energetics and equilibria in relation to exchangeable cations in faujasite, Trans. Faraday Soc. 61 (1965) 948–961, https://doi.org/10.1039/TF9656100948.
[36] K.S. Walton, M.B. Abney, M.D. LeVan, CO2 adsorption in y and X zeolites modified by alkali metal cation exchange, Microporous Mesoporous Mater. 91 (2006) 78–84, https://doi.org/10.1016/j.micromeso.2005.11.023.
[37] G.D. Pirngruber, P. Raybaud, Y. Belmabkhout, J. Čejka, A. Zukal, The role of the extra-framework cations in the adsorption of CO2 on faujasite y, Phys. Chem. Chem. Phys. 12 (2010) 13534–13546, https://doi.org/10.1039/b927476f.
[38] K.-M. Lee, Y.-H. Lim, C.-J. Park, Y.-M. Jo, Adsorption of low-level CO2 using modified zeolites and activated carbon, Ind. Eng. Chem. Res. 51 (2012) 1355–1363.
[39] G. Maurin, P.L. Llewellyn, R.G. Bell, Adsorption mechanism of carbon dioxide in faujasites: grand canonical Monte Carlo simulations and microcalorimetry measurements, J. Phys. Chem. B 109 (2005) 16084–16091.
[40] D. Bonenfant, M. Kharoune, P. Niquette, M. Mimeault, R. Hausler, Advances in principal factors influencing carbon dioxide adsorption on zeolites, Sci. Technol. Adv. Mater. 9 (2008), https://doi.org/10.1088/1468-6996/9/1/013007.
[41] P. Li, F.H. Tezel, Equilibrium and kinetic analysis of CO2-N2 adsorption separation by concentration pulse chromatography, J. Colloid Interface Sci. 313 (2007) 12–17.
[42] G. Li, P. Xiao, P.A. Webley, J. Zhang, R. Singh, Competition of CO2/H2O in adsorption based CO2 capture, Energy Procedia 1 (2009) 1123–1130.
[43] J.M. Kolle, M. Fayaz, A. Sayari, Understanding the effect of water on CO2 adsorption, Chem. Rev. 121 (2021) 7280–7345.
[44] F. Brandani, D.M. Ruthven, The effect of water on the adsorption of CO2 and C3H8 on type X zeolites, Ind. Eng. Chem. Res. 43 (2004) 8339–8344.
[45] S.U. Rege, R.T. Yang, A novel FTIR method for studying mixed gas adsorption at low concentrations: H2O and CO2 on NaX zeolite and γ-alumina, Chem. Eng. Sci. 56 (2001) 3781–3796.
[46] R.V. Siriwardane, M.-S. Shen, E.P. Fisher, Adsorption of CO2, N2, and O2 on natural zeolites, Energy & Fuels 17 (2003) 571–576.
[47] P.A. Zapata, J. Faria, M.P. Ruiz, R.E. Jentoft, D.E. Resasco, Hydrophobic zeolites for biofuel upgrading reactions at the liquid-liquid interface in water/oil emulsions, J. Am. Chem. Soc. 134 (2012) 8570–8578.
[48] H. Xiong, H.N. Pham, A.K. Datye, Hydrothermally stable heterogeneous catalysts for conversion of biorenewables, Green Chem. 16 (2014) 4627–4643.
[49] Aspen Technology, Aspen ADSIM ™ User Guide and Reference, (2000).

[50] S. Xiang, Y. He, Z. Zhang, H. Wu, W. Zhou, R. Krishna, B. Chen, Microporous metal-organic framework with potential for carbon dioxide capture at ambient conditions, Nat. Commun. 3 (2012) 954, https://doi.org/10.1038/ncomms1956.
[51] A. Masala, J.G. Vitillo, G. Mondino, C.A. Grande, R. Blom, M. Manzoli, M. Marshall, S. Bordiga, CO2 capture in dry and wet conditions in UTSA-16 metal-organic framework, ACS Appl. Mater. Interfaces 9 (2017) 455–463, https://doi.org/10.1021/acsami.6b13216.
[52] D. Xu, J. Zhang, G. Li, P. Xiao, P. Webley, Y. zhai,, Effect of water vapor from power station flue gas on CO2 capture by vacuum swing adsorption with activated carbon, J. Fuel Chem. Technol. 39 (2011) 169–174, https://doi.org/10.1016/S1872-5813(11)60016-9.
[53] K. Schumann, A. Brandt, B. Unger, EP2527296A2 Adhesive-free zeolithic granulate with faujasite structure and method for producing such an adhesive-free zeolithic granulate and use of same, EP2527296A2 (2012). https://patents.google.com/patent/EP2527296A2/en.
[54] D.D. Do, Adsorption analysis: equilibria and kinetics, World Scientific, 1998, https://doi.org/10.1142/9781860943829.
[55] D.M. Ruthven, Fundamentals of adsorption equilibrium and kinetics in microporous solids, in: Adsorption and Diffusion, Springer, 2006, pp. 1–43.
[56] F. Brandani, D. Ruthven, C.G. Coe, Measurement of adsorption equilibrium by the zero length column (ZLC) technique part 1: single-component systems, Ind. Eng. Chem. Res. 42 (2003) 1451–1461.
[57] D.M. Ruthven, Principles of Adsorption and Adsorption Processes, 1st ed., John Wiley & Sons, New York, 1984.
[58] R.T. Yang, Gas separation by adsorption processes, World Scientific, 1997.
[59] Q. Zhao, F. Wu, Y. Men, X. Fang, J. Zhao, P. Xiao, P.A. Webley, C.A. Grande, CO2 capture using a novel hybrid monolith (H-ZSM5/activated carbon) as adsorbent by combined vacuum and electric swing adsorption (VESA), Chem. Eng. J. 358 (2019) 707–717, https://doi.org/10.1016/j.cej.2018.09.196.
[60] M. Thommes, K. Kaneko, A.V. Neimark, J.P. Olivier, F. Rodriguez-Reinoso, J. Rouquerol, K.S.W. Sing, Physisorption of gases, with special reference to the evaluation of surface area and pore size distribution (IUPAC Technical Report), Pure Appl. Chem. 87 (2015) 1051–1069.
[61] W.J. Mortier, Zeolite electronegativity related to physicochemical properties, J. Catal. 55 (1978) 138–145.
[62] D.W. Ming, J.B. Dixon, Quantitative determination of clinoptilolite in soils by a cation-exchange capacity method, Clays Clay Miner. 35 (1987) 463–468.
[63] M. Katoh, T. Yoshikawa, T. Tomonari, K. Katayama, T. Tomida, Adsorption characteristics of ion-exchanged ZSM-5 zeolites for CO2/N2 mixtures, J. Colloid Interface Sci. 226 (2000) 145–150.
[64] T. Yamazaki, M. Katoh, S. Ozawa, Y. Ogino, Adsorption of CO2 over univalent cation-exchanged ZSM-5 zeolites, Mol. Phys. 80 (1993) 313–324.
[65] T. Masuda, K. Tsutsumi, H. Takahashi, Calorimetric evidence for nonspecific and specific interactions of several gases with surfaces of NaA and CaNaA zeolites, J. Colloid Interface Sci. 77 (1980) 238–242.
[66] R.M. Barrer, E.V.T. Murphy, Influence of decationation and dealumination on sorption by mordenite and clinoptilolite, J. Chem. Soc. A Inorganic, Phys. Theor. (1970) 2506–2514.
[67] B. Coughlan, S. Kilmartin, Zeolites X, Y and A enriched with trivalent cations: sorption of carbon dioxide and ammonia. Part 1. —Isotherms and affinities, J. Chem. Soc. Faraday Trans. 1 Phys. Chem. Condens. Phases 71 (1975) 1809–1817.
[68] H.W. Habgood, Adsorptive and gas chromatographic properties of various cationic forms of zeolite X, Can. J. Chem. 42 (1964) 2340–2350.
[69] A.K. Rajagopalan, A.M. Avila, A. Rajendran, Do adsorbent screening metrics predict process performance? A process optimisation based study for post-combustion capture of CO2, Int. J. Greenh. Gas Control 46 (2016) 76–85, https://doi.org/10.1016/j.ijggc.2015.12.033.
[70] J. Zhang, P.A. Webley, Cycle development and design for CO2 capture from flue gas by vacuum swing adsorption, Environ. Sci. Technol. 42 (2008) 563–569, https://doi.org/10.1021/es0706854.
[71] F.A. Da Silva, J.A. Silva, A.E. Rodrigues, A general package for the simulation of cyclic adsorption processes, Adsorption 5 (1999) 229–244.